Supporting Information

Reevaluation of Poly(ethylene-alt-propylene)-*block*-Polydimethylsiloxane Phase Behavior Uncovers Topological Close-Packing and Epitaxial Quasicrystal Growth

Aaron P. Lindsay,[1] Ashish Jayaraman,[1] Andreas J. Mueller,[1] Austin J. Peterson,[1] Steven Weigand,[3] Kristoffer Almdal,[4] Mahesh K. Mahanthappa,[1] Timothy P. Lodge,[1,2] Frank S. Bates*[1]

[1]Department of Chemical Engineering and Materials Science and [2]Department of Chemistry, University of Minnesota, Minneapolis, MN 55455, USA

[3]DND-CAT Synchrotron Research Center, Northwestern University, APS/ANL Building 432-A004, 9700 South Cass Ave, Argonne, Illinois 60439, USA

[4]Department of Chemistry, Technical University of Denmark, Kemitorvet 207, 2800 Kgs., Lyngby, Denmark

*Corresponding Author: Frank S. Bates (bates001@umn.edu)

Contents **Page**

Table S1. Molecular characteristics reported in Refs. 1 and 2

M_n[a] (kg/mol)	f_{PEP}[b]	$M_{n,PEP}$[c] (kg/mol)	$M_{n,PDMS}$[c] (kg/mol)	$Đ$[d]	N[e]	$\overline{N}$[f]
12.5	0.22	2.5	10	1.08	203	519

[a]The number average molecular weight was calculated from synthesis stoichiometry and verified *via* matrix-assisted laser desorption/ionization time-of-flight (MALDI-TOF) measurements on the precursor 1,4-polyisoprene-*block*-polydimethylsiloxane (PI-PDMS). [b]The PEP volume fraction was calculated from stoichiometry based on a reference volume (v) of 118 Å^3 and monomer densities at 140 ºC (ρ_{PEP} = 0.79 g/cm^3 and ρ_{PDMS} = 0.895 g/cm^3 from Ref. 3) and verified *via* proton nuclear magnetic resonance spectroscopy (^{1}H NMR) measurements on the precursor PI-PDMS. [c]The PEP and PDMS block molecular weights were calculated from volume fraction and number average molecular weight. [d]Molar mass dispersity (M_w/M_n) was determined *via* size exclusion chromatography in tetrahydrofuran (THF) relative to polystyrene standards. [f]The degree of polymerization was calculated for v = 118 Å^3 based on monomer densities at 140 ºC. [g]The invariant degree of polymerization was calculated as $\overline{N} = N(f_{PEP}b_{PEP}^2 + {}_{PDMS}b_{PDMS}^2)^3/v^2$, where b_{PEP} = 6.8 Å and b_{PDMS} = 5.4 Å are the block statistical segment lengths calculated at 140 ºC for v = 118 Å^3 from data in Ref. 3.

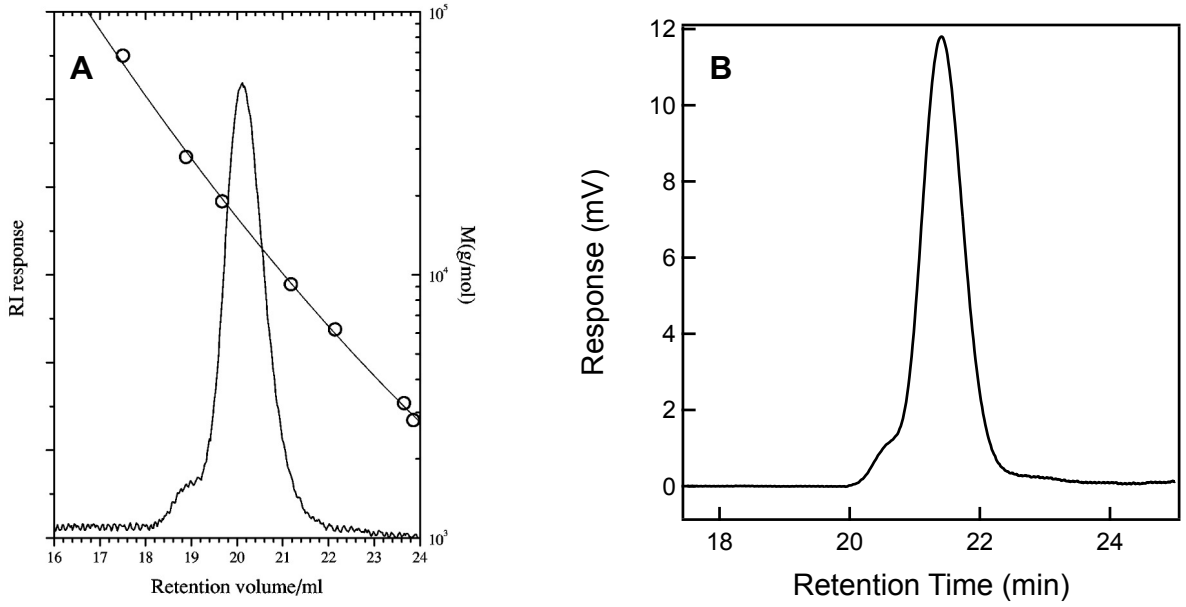

Figure S1. Comparison of size exclusion chromatography data collected in tetrahydrofuran (A) by Papadakis *et al*. and (B) in this work. (A) is reproduced from ref. 1, with the permission of AIP Publishing.

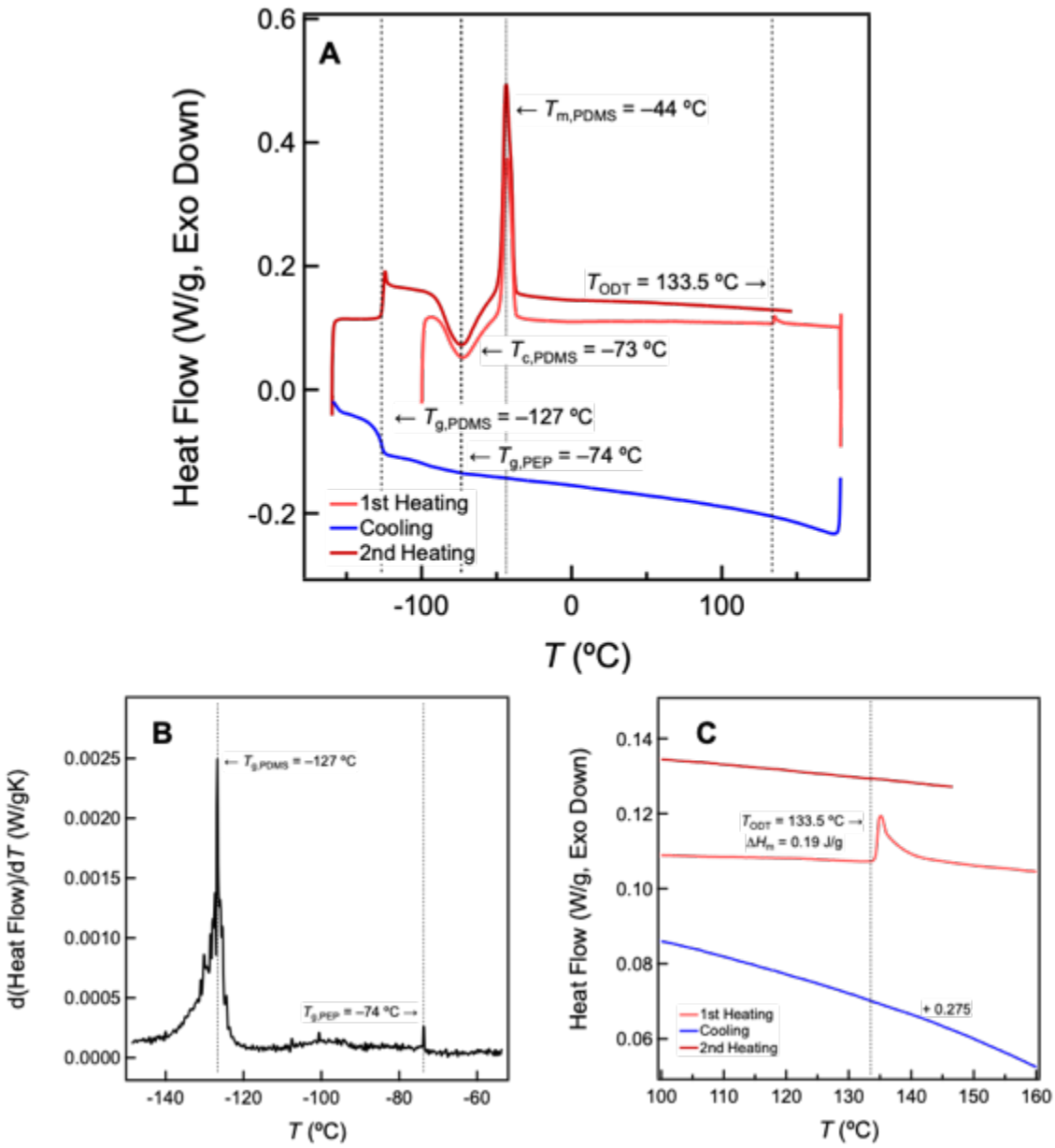

Figure S2. (A,C) Heat flow and (B) derivative of the heat flow as a function of temperature as determined *via* differential scanning calorimetry. Data were collected on heating (light red), cooling (blue), and reheating (dark red) at a ramp rate of 10 °C/min. Data in B were calculated from the cooling ramp. The endotherm on the first heating ramp in C reflects the order-disorder transition (ODT) with an enthalpy ΔH_m = 0.19 J/g determined *via* peak integration.

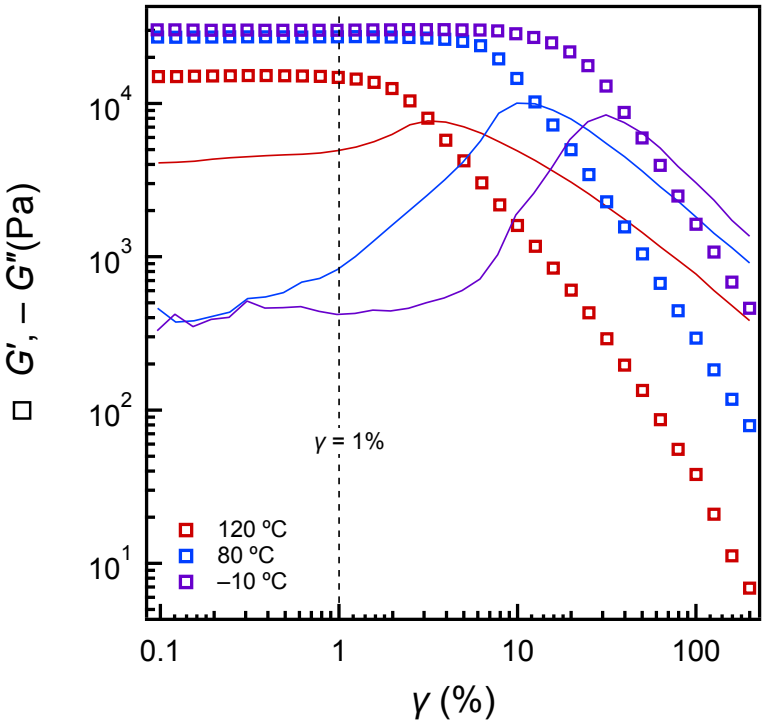

Figure S3. Strain sweep data collected *via* dynamic mechanical analysis (DMA) as a function of temperature at a constant frequency ω = 1 rad/s.

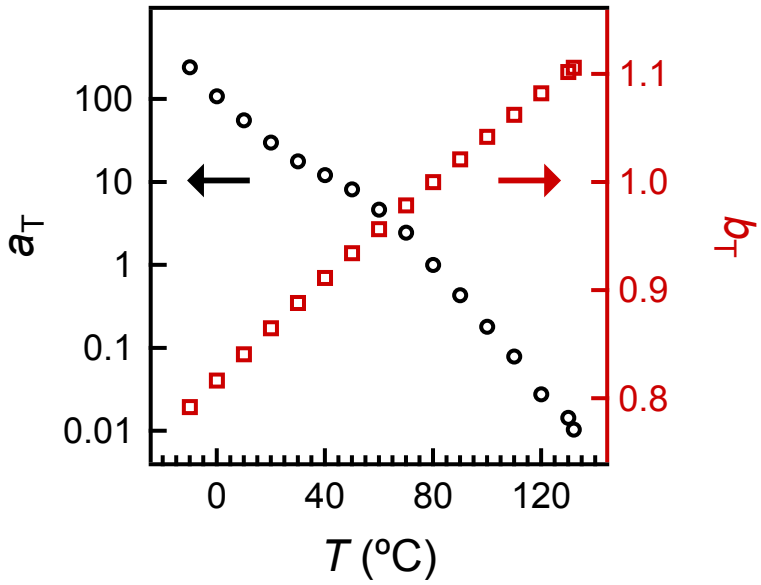

Figure S4. Time temperature superposition (TTS) horizontal (a_T) and vertical (b_T) shift factors determined for a reference temperature T_r = 80 °C. The vertical shift factor was calculated as $b_T = \rho(T)\ T\ /\ (\rho(T_r)\ T_r)$, where ρ is the density of the copolymer.

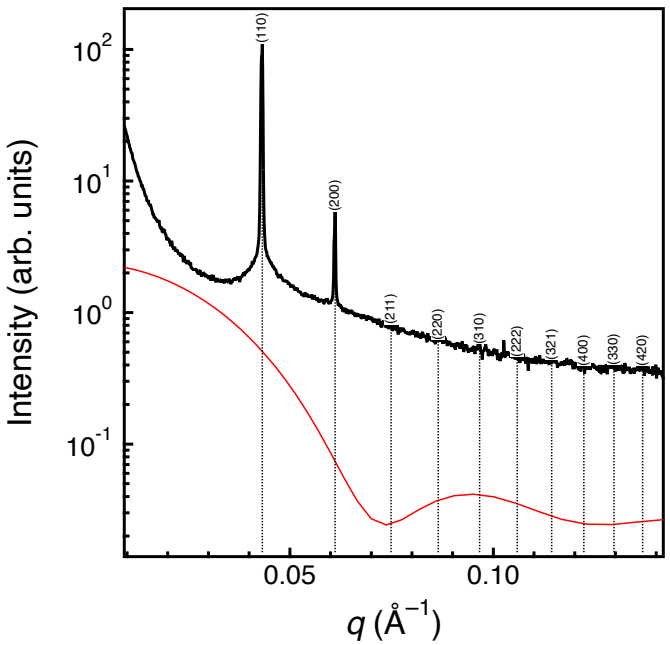

Figure S5. 1D scattering data collected following BCC shear and a 3 h anneal at 120 ºC. Dashed lines indicate expected reflections for $Im\bar{3}m$ space group symmetry and the red curve denotes the underlying spherical form-factor based on a particle radius R = 6.1 nm, calculated from the Bragg reflections as $R = 2^{1/2}3^{1/3}f^{1/3}\pi^{2/3}/q_{110}$. We anticipate a form-factor extinction of the (211) peak with higher order reflections likely missing due to thermal fluctuations near the ODT.

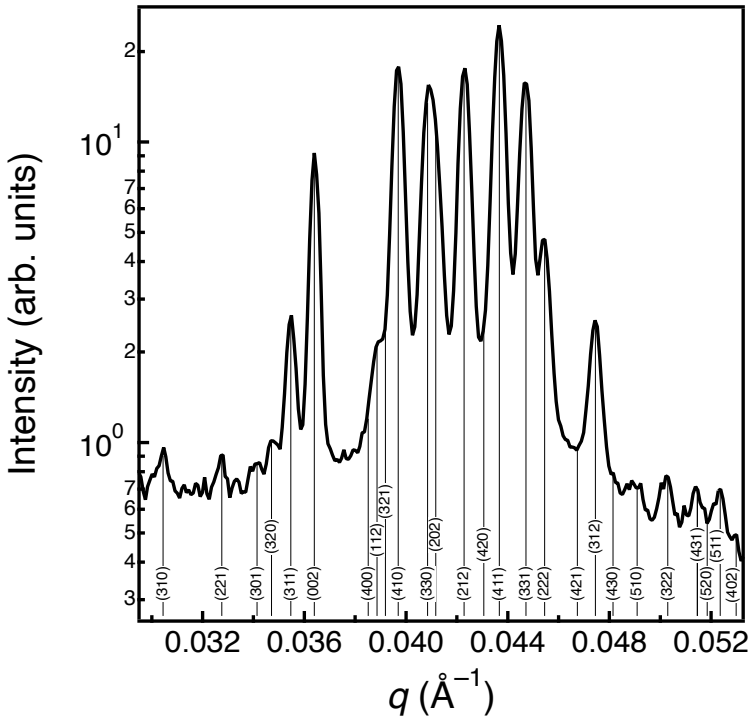

Figure S6. Fully indexed SAXS pattern for the σ phase observed after annealing at 80 ºC for 57.5 h. Further details and residuals can be found in Table S2.

Table S2. Observed and calculated peak positions for the σ phase observed after annealing at 80 ºC for 57.5 h. Peak positions were calculated as $q_{hkl} = 2\pi\,[(h^2 + k^2)/a^2 + k^2/c^2]^{1/2}$ based on $P4_2/mnm$ space group symmetry with lattice parameters a = 652.7 Å and c = 345.3 Å.

Miller Indices (*hkl*)	q_{obs} (1/Å)	q_{calc} (1/Å)	% Residual ($\Delta q/\, q_{calc} \times 100$)
(310)	0.030462	0.030442	–0.07
(221)	0.032796	0.032747	–0.15
(301)	0.034233	0.034133	–0.29
(320)	0.034771	0.034709	–0.18
(311)	0.03549	0.035465	–0.07
(002)	0.036387	0.036388	0.00
(400)	–	0.038506	–
(112)	0.038811	0.038852	0.10
(321)	–	0.039189	–
(410)	0.039709	0.039691	–0.04
(330)	0.040876	0.040842	–0.08
(202)	0.041235	0.041168	–0.16
(212)	0.042313	0.042278	–0.08
(411)	0.043660	0.043663	0.01
(331)	0.044647	0.044711	0.14
(222)	0.045455	0.045448	–0.02
(421)	–	0.046738	–
(312)	0.047430	0.047443	0.03
(430)	–	0.048133	–
(510)	0.049046	0.049086	0.08
(322)	0.050213	0.050287	0.15
(501)	0.051381	0.051457	0.15
(520)	–	0.051841	–
(511)	0.052368	0.052349	–0.04
(402)	0.052997	0.052980	–0.03

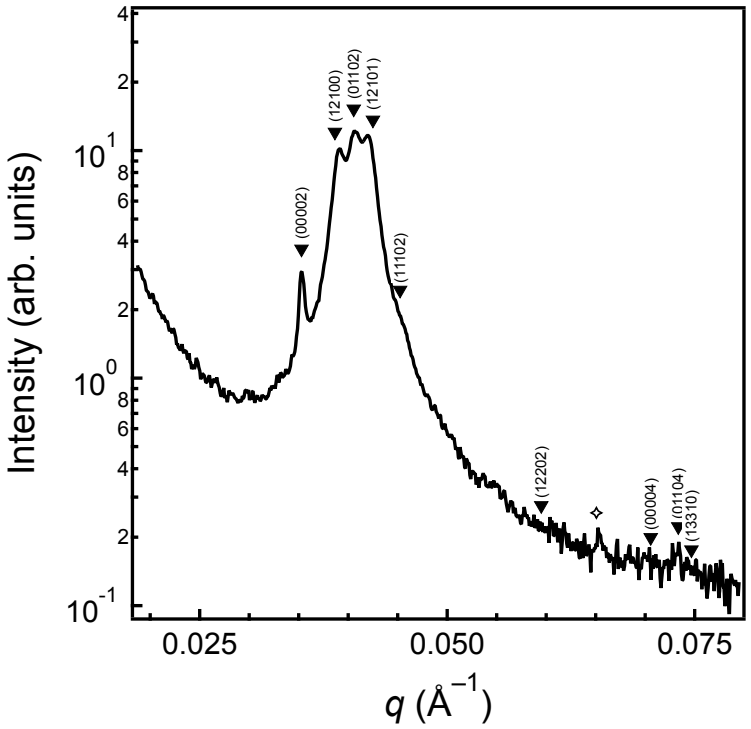

Figure S7. Fully indexed SAXS pattern for the DDQC phase observed after annealing at 40 ºC for 41 h. A satellite peak due to stray scattering is denoted by a star. Further details and residuals can be found in Table S3.

Table S3. Observed and calculated peak positions for the DDQC phase observed after annealing at 40 ºC for 41 h. Peak positions were calculated as described by Iwami and Ishimasa[4] with a tiling edge length a = 350.3 Å and periodicity c = 356.3 Å.

Miller Indices ($a_1\,a_2\,a_3\,a_4\,a_5$)	q_{obs} (1/Å)	q_{calc} (1/Å)	% Residual ($\Delta q/\,q_{calc} \times 100$)
(00002)	0.035310	0.035270	0.11
(12100)	0.039081	0.038644	1.13
(01102)	0.040607	0.040548	0.15
(12101)	0.041954	0.042478	–1.23
(11102)	0.045545	0.045214	0.73
(12202)	–	0.059478	–
(00004)	–	0.070540	–
(01104)	0.073376	0.073321	0.07
(13310)	–	0.074655	–

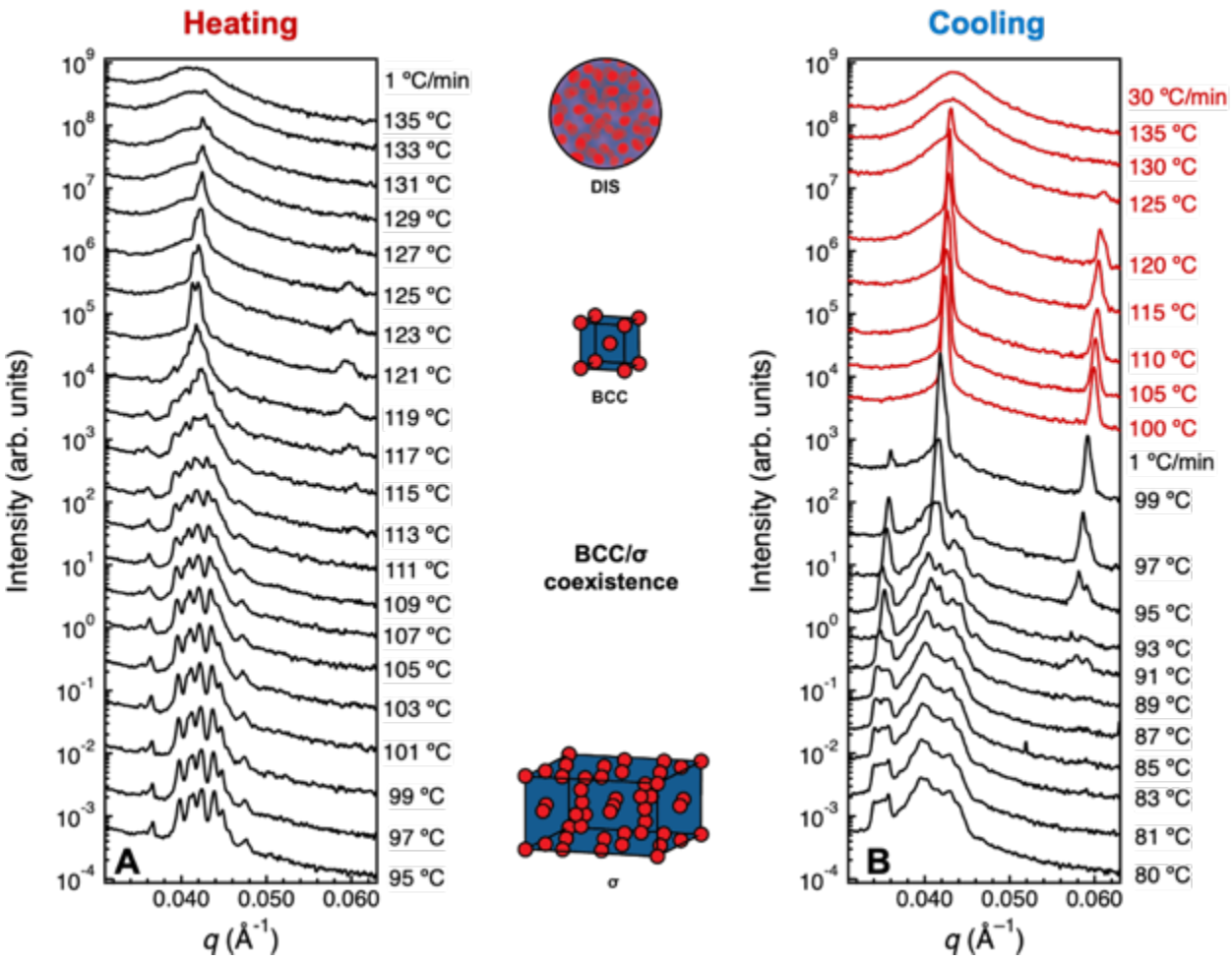

Figure S8. 1D SAXS profiles on (A) heating a σ phase and (B) cooling a BCC packing at 1 ºC/min. The σ phase was obtained on annealing at 95 ºC for 35 min and the BCC phase was obtained on cooling from 140 ºC at 30 ºC/min.

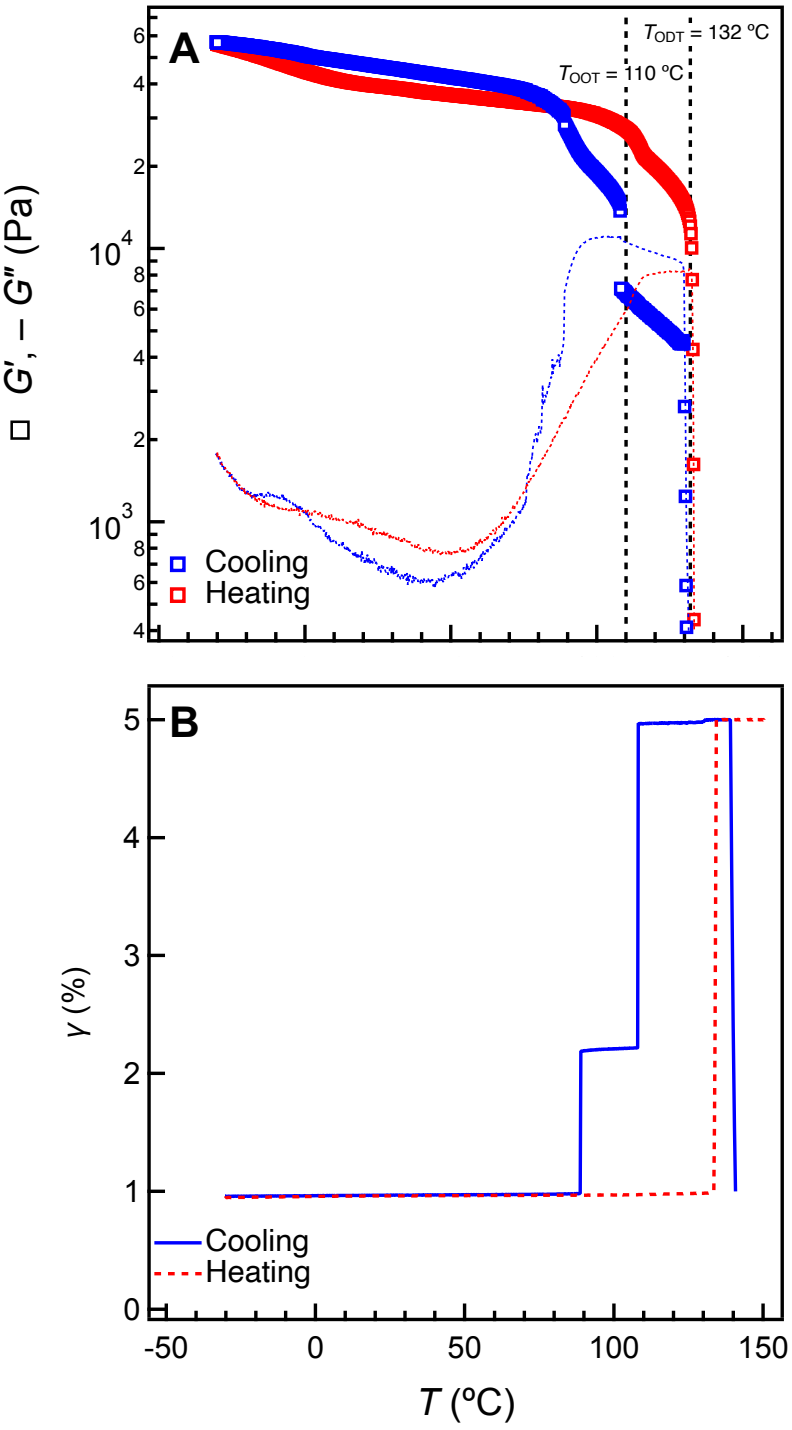

Figure S9. (A) Isochronal (1 rad/s) temperature ramp data collected *via* DMA with (B) variable strain on cooling (blue) and subsequent heating (red) at a rate of 1 ºC/min. Discrepancies in the magnitude of G' in (A) on heating and cooling are partially a consequence of a variable strain amplitude (B), which pushed measurements outside of the LVE regime within the BCC window on cooling. The arrow in (A) highlights the transition at 120 ºC observed on heating.

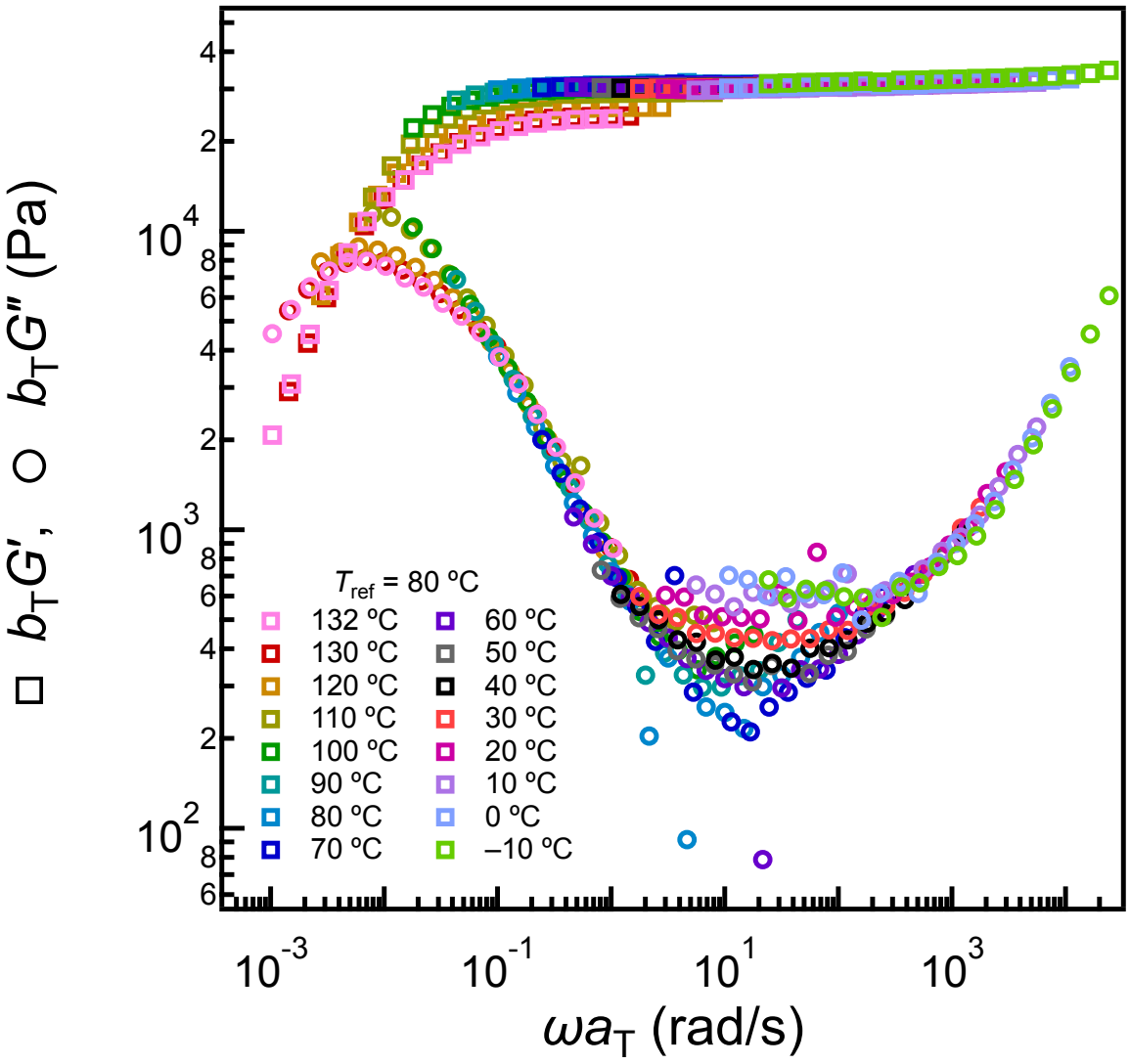

Figure S10. Frequency sweep data collected *via* DMA on heating at 0.2 ºC/min and 1% strain. Data was shifted horizontally by a factor a_T according to the time-temperature superposition (TTS) principle. Data was also vertically shifted by a factor $b_T = \rho(T)\ T\ /\ (\rho(T_r)\ T_r)$, where ρ is the density of the copolymer and T_r = 80 ºC was the chosen reference temperature. Shift factors can be found in Figure S4.

Calculation of mean particle radii:

The mean particle radii $\langle R \rangle$ can be calculated as:

$$\langle R \rangle = \left(\frac{3V_{UC}}{4\pi\rho_{P,UC}} \right)^{1/3} \quad \text{(S1)}$$

where V_{UC} is the unit cell volume determined from SAXS data and $\rho_{P,UC}$ is the known number of particles per unit cell. For the BCC phase, this yields:

$$\langle R \rangle_{BCC} = R_{BCC} = \frac{3^{1/3}2^{1/2}\pi^{2/3}}{q_{110}} \quad \text{(S2)}$$

where $\langle R \rangle_{BCC} = R_{BCC}$ due to the unimodal particle size distribution and q_{110} corresponds to the position of the principal scattering reflection. For the σ phase, this translates to:

$$\langle R \rangle_{\sigma} = \frac{2\pi^{2/3}}{5^{1/3}(c/a)^{2/3}q_{002}} \quad \text{(S3)}$$

where (c/a) is the ratio of the unit cell parameters for the tetragonal lattice ($c/a \approx 0.53$) and q_{002} is the scattering wavevector associated with the spacing between (002) planes. Due to the absence of translational symmetry, a similar calculation is not possible for a DDQC. However, the mean particle size is not expected to differ significantly on passing through the DDQC/σ OOT. This is due to the close structural relationship of the phases and the universal invariance in the spacing between dense and sparse planes reflected in the equivalence of the q_{00002} and q_{002} scattering reflections on transitioning from a DDQC to a σ phase. As such, the mean particle radius can be estimated *via* Equation S3 upon substituting q_{002} with q_{00002}.

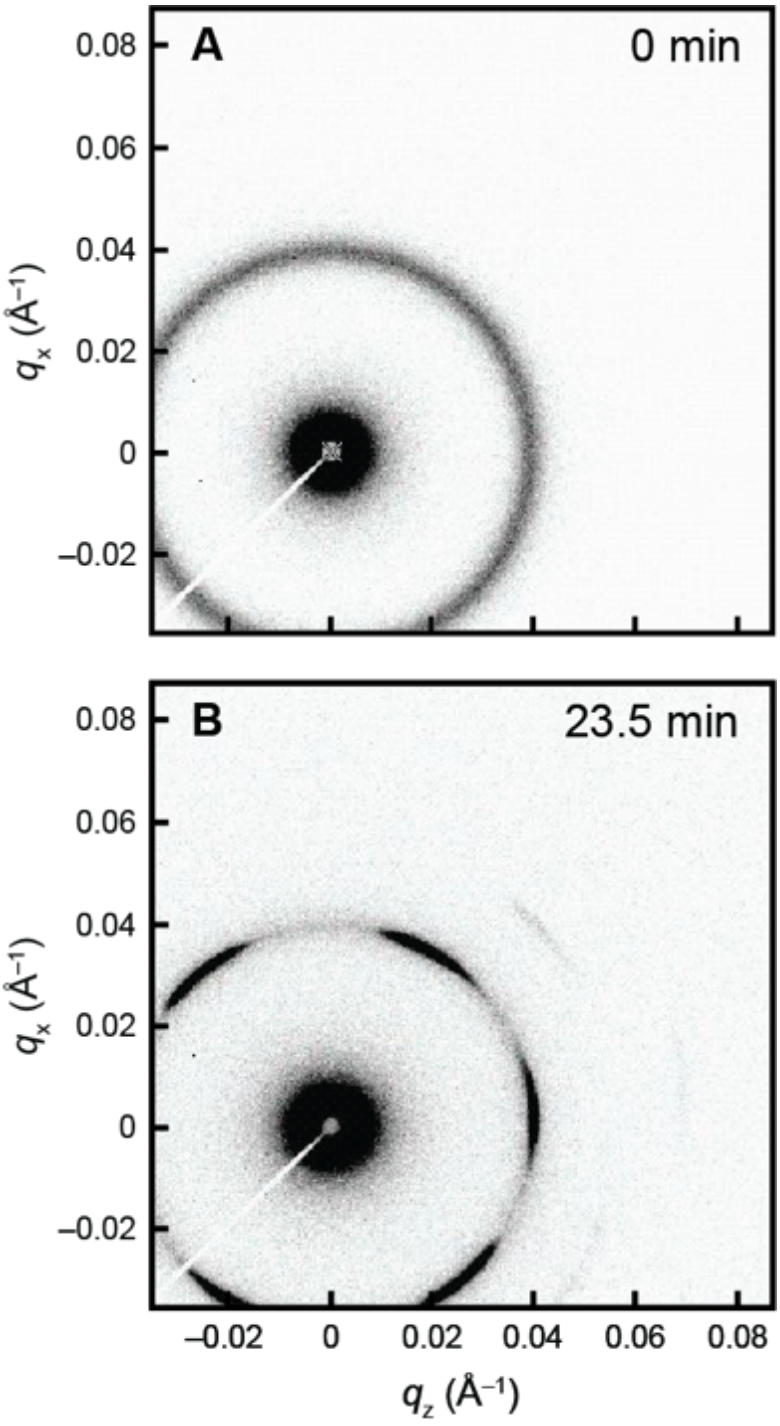

Figure S11. 2D Scattering data obtained (A) on cooling the as-loaded sample from 150 ºC to –10 ºC and (B) after 23.5 min of subsequent shear (γ = 106.2%, ω = 9.9 Hz).

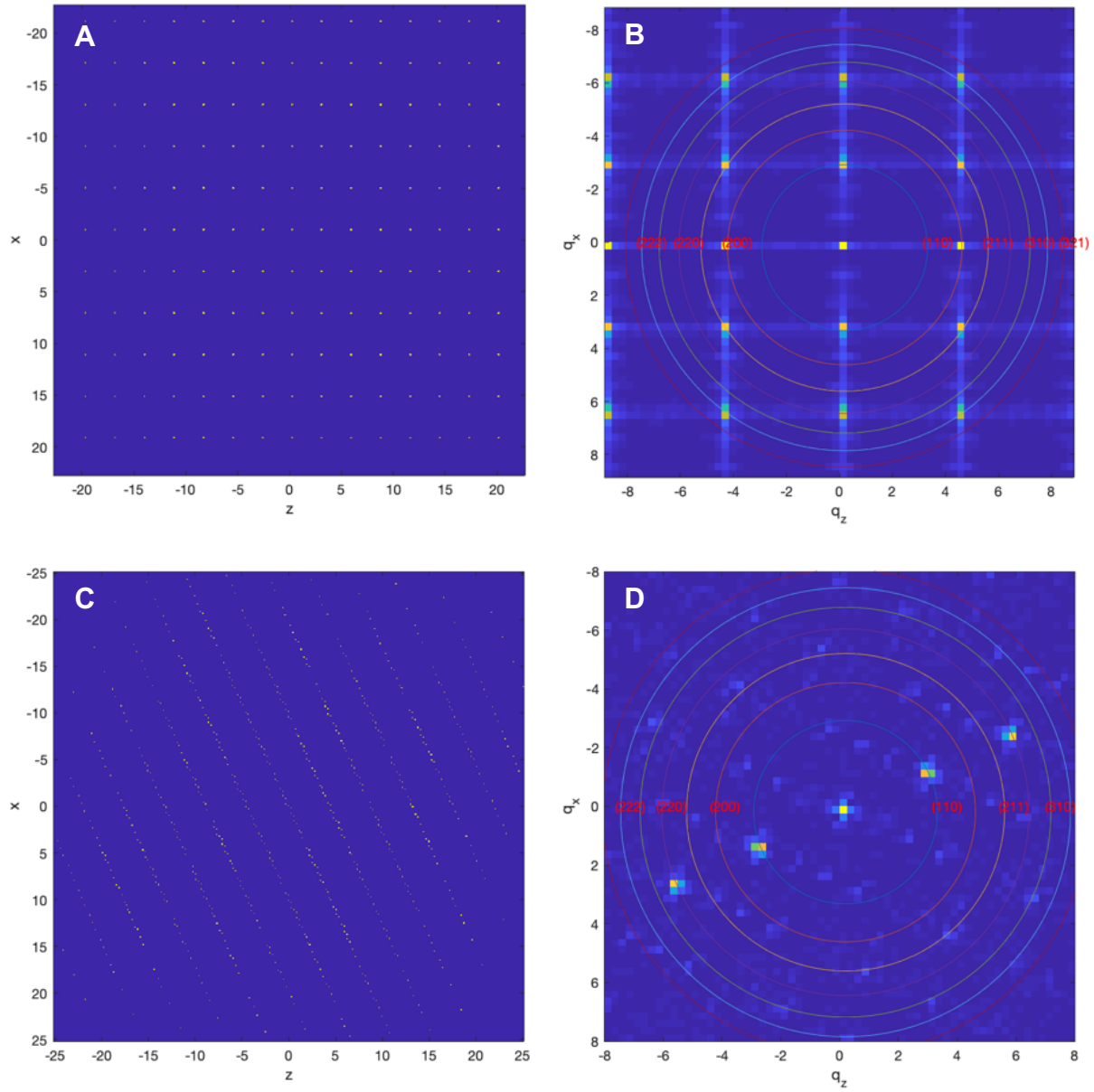

Figure S12. Simulated (B,D) 2D diffraction patterns and (A,C) corresponding real space projections for (A,B) the BCC (110) oriented perpendicular to the incident beam and (C,D) on a 30º rotation about the *x*-axis. Simulated diffraction patterns were calculated *via* a Fourier transform of the real space images.

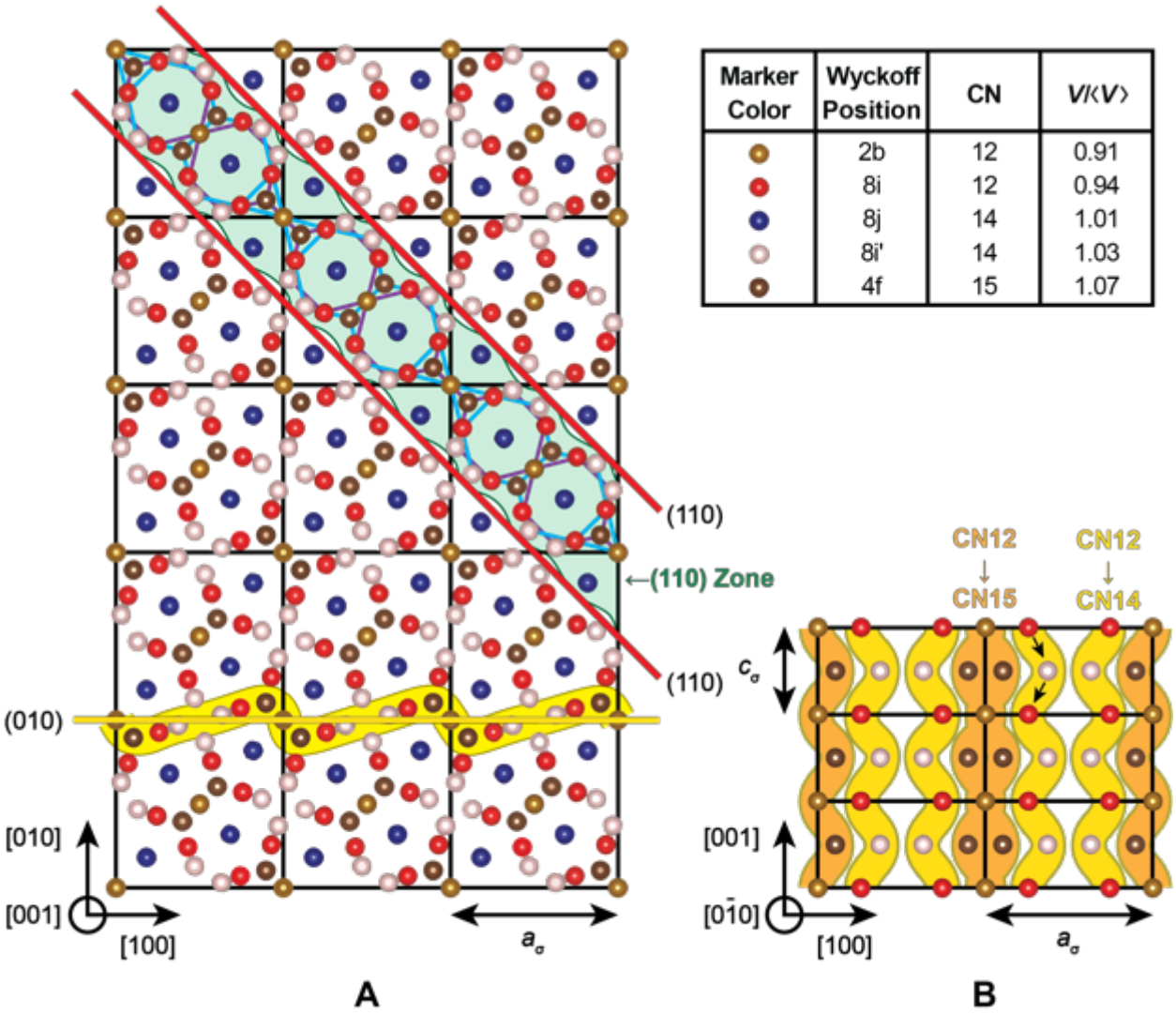

Figure S13. Illustration of slip systems identified for the FK σ phase relative to the (A) (001) and (B) (0$\bar{1}$0) planes. In (A), the (110) zone identified by Kronberg is shaded green and the Kagomé tilings constituting the B and C layers of the ABACABAC… stacking of (001) planes are outlined in blue and purple, respectively. A detailed description of Kronberg's zonal dislocation can be found in the original text [5]. Atoms involved in the {100}⟨001⟩ slip system are highlighted in yellow in (A). The view of these atoms in (0$\bar{1}$0) plane is shown in (B) wherein the orange and yellow shadings highlight the CN 12→15 and CN 12→14 slip pathways, respectively, that were identified by Rodriguez and Coll [6]. Note that the blue atoms in (A) make up the sparse "A" planes and are omitted from (B) since they are not involved in the proposed slip mechanism. The values in the upper right table were calculated from data in Ref. [7]. (A,B) were adapted from unit cells constructed in Vesta [8].

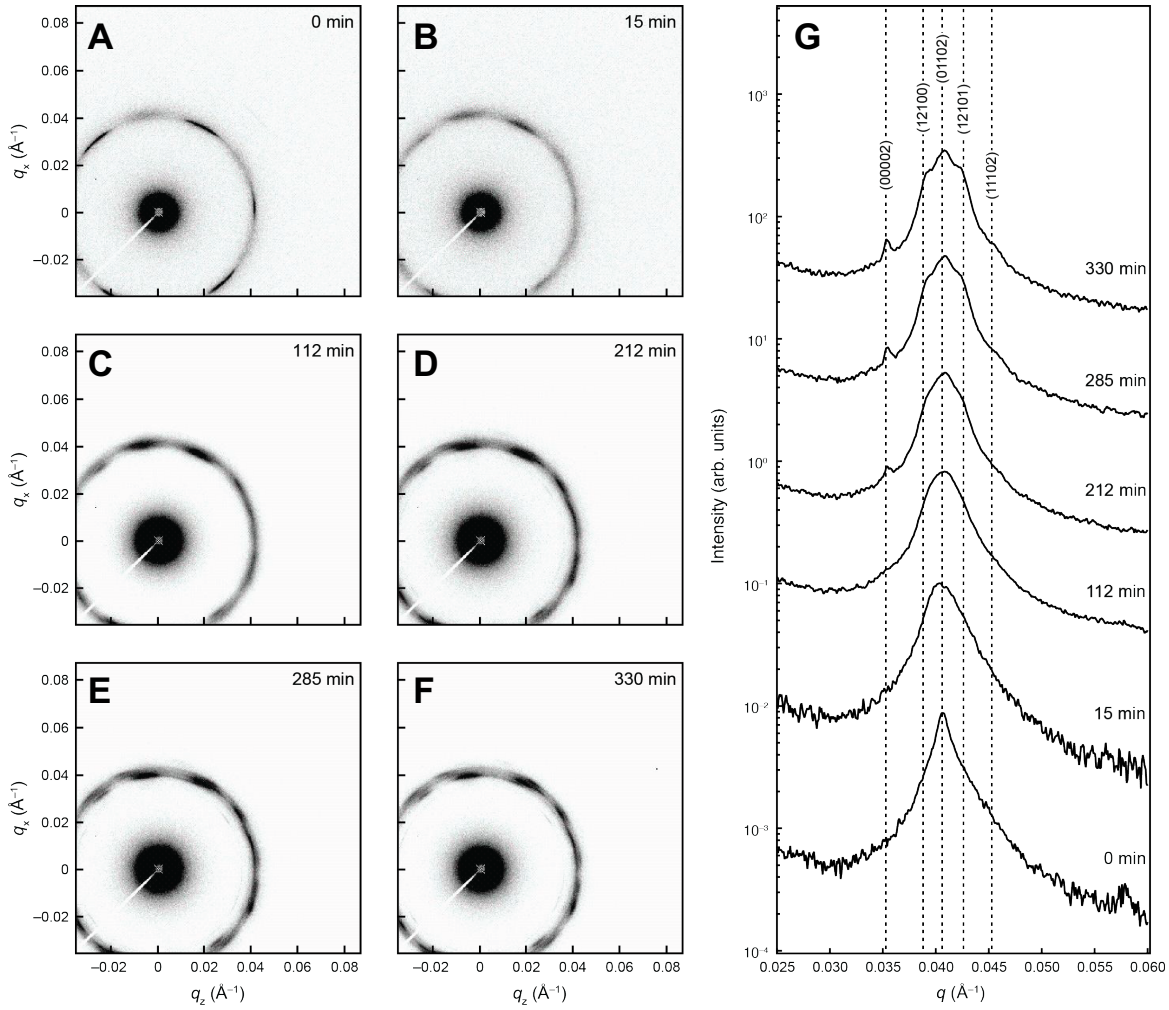

Figure S14. (A-F) 2D scattering patterns collected over time at 50 ºC after heating the shear-oriented sample in Figures 6 and S11, where time 0 corresponds to the time at which the sample reached 50 ºC. The corresponding 1D scattering profiles are provided in (G).

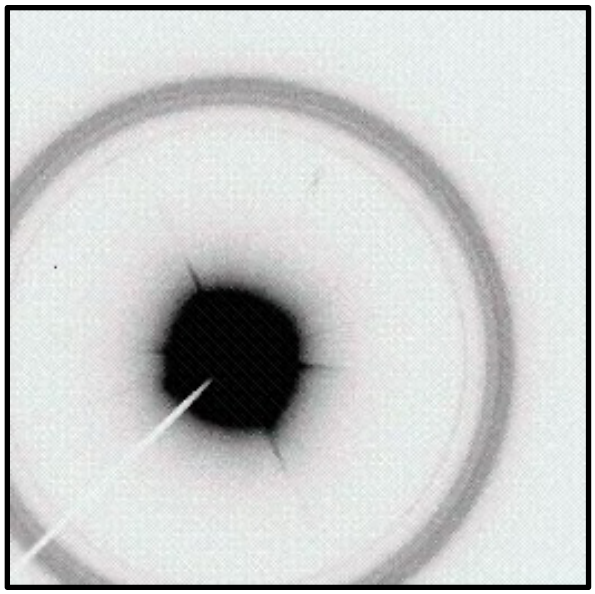

Figure S15. 2D scattering pattern for a DDQC obtained after 41 h of annealing at 40 ºC without shear.

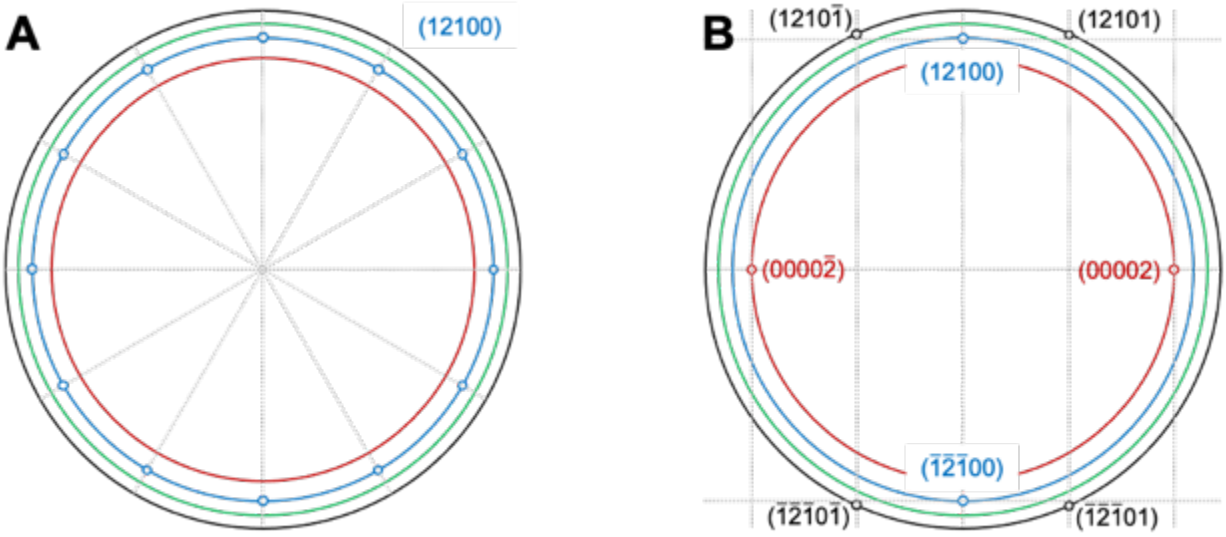

Figure S16. Calculated 2D diffraction patterns for a DDQC with the 12-fold axis oriented (A) parallel and (B) perpendicular to the incident beam. Red, blue, green, and black concentric circles correspond to q_{00002}, q_{12100}, q_{01102}, and q_{12101}, respectively.

Estimation of error in BCC/DDQC epitaxy:

The intermicellar spacing of the sparse planes of the dodecagonal quasicrystal (DDQC) ($d_{\text{sparse,DDQC}}$) is the just the edge length a_{QC} associated with the square and triangle tiling motif. However, for the dense planes, we estimate the intermicellar spacing as the spacing between centroids of two adjacent triangle tilings sharing one edge. The distance h from the centroid to the shared edge of an equilateral triangle can be calculated as $h = \tan(30^{\text{o}})/2\ a_{\text{QC}}$. Therefore, we can estimate the spacing between the two triangle centroids and thus the intermicellar spacing in the densely packed planes as $d_{\text{dense,QC}} = \sqrt{(3)}/3\ a_{\text{QC}}$.

For the BCC (110) plane, shown in Figure 8B, there are multiple dimensions that could be associated with the intermicellar spacing of the dense and sparse planes of a future DDQC packing. The intermicellar spacing related to the future sparse planes is just the long edge length of the 2D rectangular lattice in the (110) plane (*i.e.*, the face diagonal), making $d_{\text{sparse,BCC(110)}} = \sqrt{(2)}\ a_{\text{BCC}}$. For the dense planes, the distorted hexagonal motif is characterized by $d_{\text{dense,BCC(110)}} = a_{\text{BCC}}$ or $d_{\text{dense,BCC(110)}} = \sqrt{(3)}/2\ a_{\text{BCC}}$ (*i.e.*, the atomic spacing in the [111] direction).

For the BCC (111) plane, the intermicellar spacing of the posited future sparse planes corresponds to the edge length of the triangle in Figure 8C (*i.e.*, the face diagonal), which can be calculated as $\sqrt{(2)}\ a_{\text{BCC}}$ *via* the Pythagorean theorem. Neglecting the out-of-plane displacement, we calculate the intermicellar spacing in the "dense" plane (blue points in Figure 8) in a manner analogous to the calculation done above for the DDQC, but with a shared edge length of $\sqrt{(2)}/2$. This yields $d_{\text{dense,BCC(111)}} = \sqrt{(6)}/3\ a_{\text{BCC}}$.

Using above relations, we can estimate the error in the potential epitaxy as $(d_{i,\text{QC}} - d_{i,j})/d_{i,\text{QC}} \times 100\%$, where i corresponds to the intermicellar distance is in the dense or sparse planes and j corresponds to either the BCC (110) or (111) planes, neglecting out-of-plane error. As noted in the text, based on the scattering data, which reflected a constant mean particle radius, the ratio of

the DDQC tiling edge length to the BCC lattice parameter is $a_{QC}/a_{BCC} = 1.6$. The resulting errors are listed in Table S4.

Table S4. Calculated error between the packing in the 12-fold DDQC plane and the BCC (110) and (111) planes.

BCC plane (*hkl*)	"Dense" plane error (%)	"Sparse" plane error (%)
(110)	–2.1 ± 7.3[a]	10.7
(111)	10.7	10.7

[a]The uncertainty reflects the maximum and minimum errors.

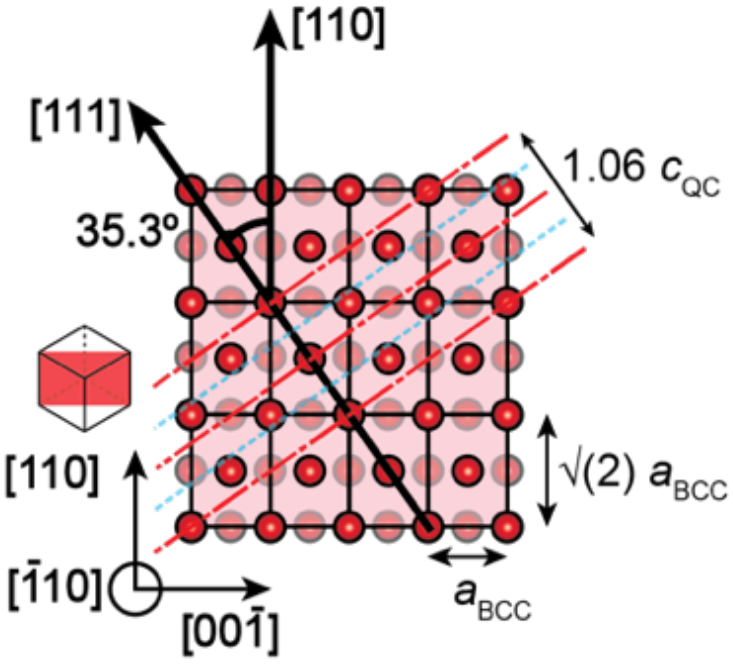

Figure S17. Proposed orientation of growing DDQC relative to BCC (110) plane, where red and blue lines are associated with the spacing and orientation of the sparse and dense planes, respectively, of the DDQC as shown in Figure 8D.

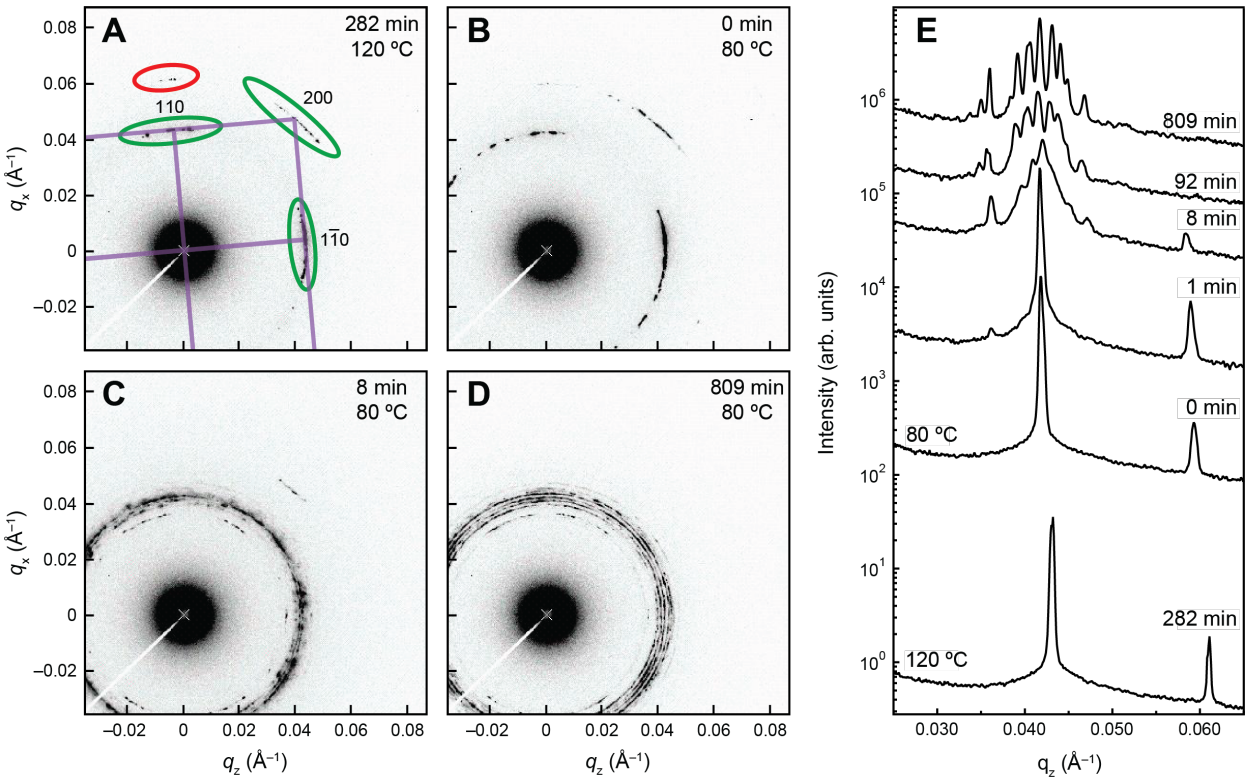

Figure S18. Scattering data collected on cooling a shear-oriented high temperature BCC phase into the σ phase window. The as-loaded sample was disordered at 150 ºC and cooled to 120 ºC before applying steady and large amplitude oscillatory shear. Orientation was observed following 46.5 min of large amplitude oscillatory shear (γ = 106.2%, ω = 9.9 Hz) and the sample was left to anneal for 3 h (cumulatively 282 min at 120 ºC) prior to collection of the 2D scattering pattern in (A). The scattering pattern was indexed to a (100) reciprocal lattice (purple) as noted in the main text. An additional scattering reflection at q_{200} owing to the limited orientation of the pattern is denoted by a red oval. 2D scattering patterns in (B-D) were collected on cooling the oriented BCC structure from 120 ºC to 80 ºC at a rate of 30 ºC/min and annealing for 0, 8, and 809 min. Corresponding 1D SAXS patterns are shown in (E) where time 0 corresponds to the time at which the sample reached each temperature.

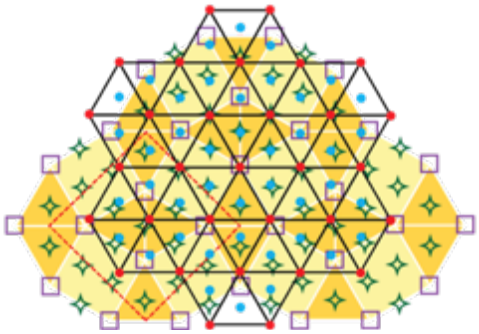

Figure S19. Coincidence site lattice model for the σ (001) and BCC (111) planes. Red circles correspond to micelles within each respective BCC plane, whereas puckered green diamonds and purple squares correspond to the location of micelles within the dense and sparse σ planes. Blue circles correspond to the packing in subsequent BCC (111) planes. The dashed red line denotes a single σ unit cell.

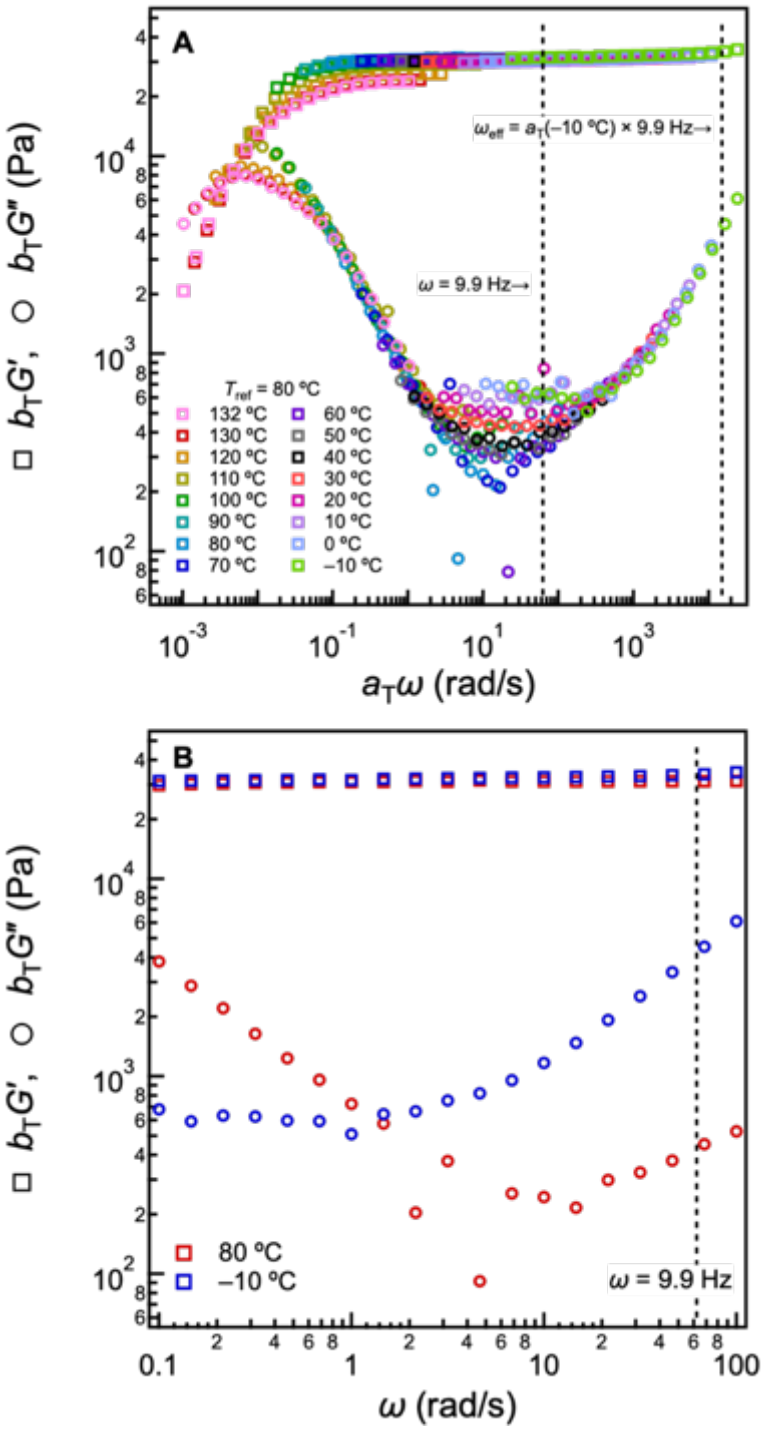

Figure S20. Comparison of the dynamic regimes probed for ω = 9.9 Hz and γ = 1% at 80 ºC and –10 ºC in (A) shifted and (B) unshifted frequency sweep data collected *via* DMA, where ω_{eff} is the effective frequency at –10 ºC in relation to the measurement at 80 ºC. (A) was reproduced from Figure S10.

References

(1) Papadakis, C. M.; Almdal, K.; Mortensen, K.; Vigild, M. E.; Štěpánek, P. Unexpected Phase Behavior of an Asymmetric Diblock Copolymer. *J. Chem. Phys.* **1999**, *111*, 4319–4326. https://doi.org/10.1063/1.479730.

(2) Vigild, M. E. Mesomorphic Phase Behaviour of Low Molar Mass PEP-PDMS Diblock Copolymers Synthesized by Anionic Polymerization. Ph.D. Thesis, University of Copenhagen, Copenhagen, Denmark, 1997.

(3) Fetters, L. J.; Lohse, D. J.; Richter, D.; Witten, T. A.; Zirkel, A. Connection between Polymer Molecular Weight, Density, Chain Dimensions, and Melt Viscoelastic Properties. *Macromolecules* **1994**, *27*, 4639–4647. https://doi.org/10.1021/ma00095a001.

(4) Iwami, S.; Ishimasa, T. Dodecagonal Quasicrystal in Mn-Based Quaternary Alloys Containing Cr, Ni and Si. *Philos. Mag. Lett.* **2015**, *95*, 229–236. https://doi.org/10.1080/09500839.2015.1038332.

(5) Kronberg, M. L. Atom Movements and Dislocation Structures for Plastic Slip in Single Crystals of β-Uranium. *J. Nucl. Mater.* **1959**, *1*, 85–95. https://doi.org/10.1016/0022-3115(59)90013-3.

(6) Rodriguez, C.; Coll, J. A. Deformation Mechanisms of β Uranium Single Crystals. *J. Nucl. Mater.* **1964**, *11*, 212–219. https://doi.org/10.1007/978-3-662-08734-3_3.

(7) Kim, K.; Schulze, M. W.; Arora, A.; Lewis, R. M.; Hillmyer, M. A.; Dorfman, K. D.; Bates, F. S. Thermal Processing of Diblock Copolymer Melts Mimics Metallurgy. *Science* **2017**, *356*, 520–523. https://doi.org/10.1126/science.aam7212.

(8) Momma, K.; Izumi, F. VESTA 3 for Three-Dimensional Visualization of Crystal, Volumetric and Morphology Data. *J. Appl. Crystallogr.* **2011**, *44*, 1272–1276. https://doi.org/10.1107/S0021889811038970.